Dynamics of Atmospheres and Oceans
37 (2003) 155–170

dynamics of atmospheres and oceans

www.elsevier.com/locate/dynatmoce

Stratified flow over asymmetric and double bell-shaped obstacles

Balázs Gyüre [a], Imre M. Jánosi [a,b,*]

[a] *von Kármán Laboratory for Environmental Flows, Eötvös University, Pázmány Péter Sétány 1/A, H-1117 Budapest, Hungary*

[b] *Department of Physics of Complex Systems, Eötvös University, Pázmány Péter Sétány 1/A, H-1117 Budapest, Hungary*

Received 10 January 2003; accepted 23 May 2003

Abstract

We performed experiments on quasi-two-dimensional lee-wave formation behind obstacles towed through a linearly stratified fluid. Initial transient times, amplitudes and wavelengths are measured for five different obstacle shapes at several flow velocities. We found that the wave field is determined primarily by the height and the leeward slope of the obstacle, in agreement with previous works. Differences between measured quantities and predictions of linear theories indicate that nonlinear effects are important in our parameter range. Experiments with a twin obstacle gave surprising results: average wavelengths and amplitudes are systematically lower than that of produced by an isolated obstacle, which we attribute to the dominance of essential nonlinearities such as anomalously strong wave dispersion.

Keywords: Stratified flow; Lee-waves; Resonant wave interaction; Laboratory experiments

1. Introduction

Internal gravity waves of topographic origin are ubiquitous in the stably stratified atmosphere and oceans. Upward-propagating lee-waves at around stationary lenticular clouds in mountain ranges were discovered by glider pilots in 1933 (Whelan, 2000). Direct field observations of the lower atmosphere (for a review see Röttger, 2000) revealed that a broad spectrum of topographically generated disturbances exists besides the most impressive quasi-stationary waves indicated by periodic cloud bands. Nevertheless, an improved understanding of atmospheric complexity is possible only through detailed analyses of

* Corresponding author. Tel.: +36-1-372-2878; fax: +36-1-372-2866.
E-mail address: janosi@lecso.elte.hu (I.M. Jánosi).

0377-0265/$ – see front matter © 2003 Elsevier B.V. All rights reserved.
doi:10.1016/S0377-0265(03)00030-7

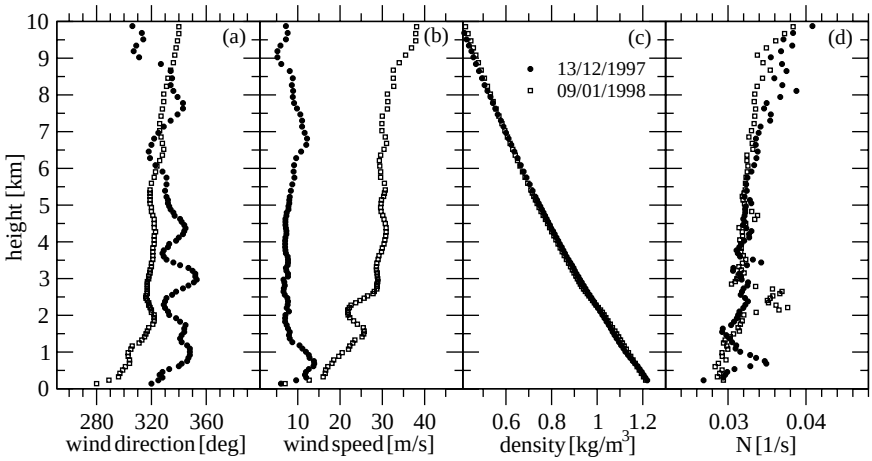

Fig. 1. Wind direction (a), wind speed (b), air density (c), and Brunt-Väisäla frequency profiles (d) for 2 days in the winter of 1997–1998 close to mountain Pilis, Hungary (latitude: 47.7°N; longitude: 18.8°E; highest altitude: 757 m).

the basic situations. Uniform flow over two-dimensional obstacles represents the simplest related model system which has been studied extensively since the pioneering works of Lyra (1943), Queney (1948), Scorer (1949), and Long (1953, 1955). It is not immediately obvious that such a simplified description might have any environmental relevance. Fig. 1 illustrates, however, that in some cases the lower atmosphere possesses nearly ideal physical properties: almost uniform wind from a constant direction in a stable stratification with an approximately constant Brunt-Väisäla frequency. Indeed, during these days wave-gliders succeeded to ascend very high at the lee side of mountain Pilis (four of the flights exceeded the height of 6 km, the best of them was 7300 m), in spite of the fact that the highest peak at this area has an elevation of 623 m only.

Several aspects of internal wave generation by topographic effects are thoroughly reviewed in monographs by Scorer (1978), Turner (1979), and especially Baines (1995). Atmospheric peculiarities are recently summarized by Nappo (2002). Laboratory simulations in towing tanks provide an attractive alternative to full-scale field experiments, moreover, they are used to benchmark analytical and numerical results. Here, we concentrate on two particular aspects of orographic waves: the effects of asymmetric obstacle shapes and the wave generation by two neighboring “mountains”. Asymmetric obstacles were experimentally investigated by Baines and Hoinka (1985), and recently by Sutherland (2002). Much more experiments were performed by symmetric objects with a wide range of geometric aspect ratios (see Baines, 1995). Numerical studies by Lilly and Klemp (1979), Baines and Granek (1990), and Garner (1995) focused on the wave drag and critical Froude number, where wave breaking occurs, as a function of asymmetry. Interestingly, lee-wave interference phenomena at the presence of two adjacent ridges are described qualitatively many times (see Scorer, 1978), however, a closer investigation has been started only recently by means of analytical (Grisogono et al., 1993) and numerical tools (Vosper, 1996; Mayr and

Gohm, 2000). The extra difficulty is clearly the huge number of possible coupling of two obstacles with various shapes and sizes. More detailed comparison of our observations with earlier results is given in Section 4, Section 2 presents the details of experiments, the results are summarized in Section 3.

2. Experimental

2.1. Apparatus

Experiments are performed in a Plexiglass tank (length: 240 cm; width: 8.7 cm; height: 40 cm) filled with uniformly stratified fluid to a depth of 35–37 cm by the standard double-bucket method (Fortuin, 1960). Food dye was periodically added up to the mixture at the filler nozzle resulting in a horizontally layered coloring. Disturbances are generated by towing an obstacle with a tense wire along the bottom of the tank from one end to the other. Five different obstacles of width 8.4 cm were tested, their cross-sectional geometry is illustrated in Fig. 2. The curved shapes obey a generalized Gaussian form

$$z(x) = a \exp(-b|x|^{2\gamma}), \tag{1}$$

with the following parameter values, where a and x are measured in mm (see Fig. 2). "A": $a = 20$, $b = 11.90 \times 10^{-4}$, $\gamma = 1$ (pure Gaussian); "B": the left side is identical with "A", the right side is linear of slope 0.125; "C": $a = 40$, $b = 1.12 \times 10^{-4}$, $\gamma = 1.36$; "D": $a = 40$, $b = 1.89 \times 10^{-4}$, $\gamma = 1.21$ (left side), and $b = 9.39 \times 10^{-4}$, $\gamma = 0.76$ (right side). The fifth obstacle ("E") is formed by two hills of shape "A" joined up with a center-to-center distance of 20 cm. In a typical experiment, the obstacle was towed to the middle of the tank until a quasi-steady state was reached, then the second half of the tow was recorded by a video camera.

Since the width of the channel (8.7 cm) in which our experiments were run is much narrower than used by other workers (apart from the ingenious apparatus constructed by Baines and Hoinka (1985) with a working width of 8.75 cm), it is worth to mention that we did not observe any effect that could be attributed to viscous friction at the sidewalls, such as

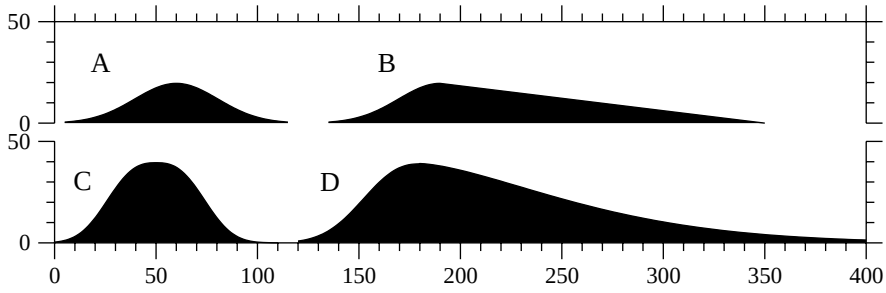

Fig. 2. Cross-sections of the towed obstacles (see Eq. (1)), the axes are scaled in units of mm. A fifth obstacle ("E" in the following) was created by joining up two hills "A" with a crest-to-crest distance of 20.0 cm.

smearing of dye bands or lagging of waves behind the obstacle. Qiu and Xia (1998) carefully measured the viscous boundary layer thickness at the sidewalls of a convection cell made of Plexiglass and using water at around room temperature. At a characteristic flow velocity ∼1 cm/s (like in our experiments), they obtained a thickness ∼2.5 mm, which is comparable with the gap between our obstacles and the sidewall (1.5 mm). Further indication of weak viscous friction was that we had to wait 20–25 min after a towing run until all visible wavy disturbances died out.

2.2. Similarity considerations

The similarity criteria which must be met in small-scale towing tank experiments have been reviewed by Baines and Manins (1989). The relevant physical quantities are the towing speed U, the fluid depth D, the uniform buoyancy (or Brunt-Väisälä) frequency $N = \sqrt{-(g/\rho)\partial_z \rho}$, the maximum obstacle height h, the obstacle half-width scale w, and the kinematic viscosity ν. The half-width w for the forms of Eq. (1) is given by the points of inflection as

$$w = \left(\frac{2\gamma - 1}{2b\gamma}\right)^{1/2\gamma}. \tag{2}$$

In case of an asymmetric obstacle w is replaced by w_u and w_d for upstream and downstream values, respectively. These quantities give the dimensionless numbers U/ND, $U/N2w$, and U/Nh related to wave propagation, wave drag, and horizontal perturbation velocity, respectively. (The last number is often called as vertical Froude number, a term criticized by Baines (1995).) The role of viscous effects are estimated by the vertical and horizontal Reynolds numbers $Re_v = Uh/\nu$, and $Re_h = U2w/\nu$, geometrical similarity can be expressed by the ratios h/D, and h/w.

By taking typical towing speeds $U = 1$–15 cm/s, measured buoyancy frequency values in the experiments $N_{exp} = 1.09$–$1.55\,s^{-1}$ and for the atmosphere $N_{atm} = 0.03$–$0.04\,s^{-1}$ (see Fig. 1), and the geometrical data listed in Section 2.1, the matching of dimensionless numbers indicates that our setup simulates atmospheric flow up to a level of 5–10 km at an obstacle height of 600 m for uniform wind speed in the range of 10–70 m/s. Obviously, the Reynolds numbers in the experiments ($Re_{exp} \approx 10^2$–10^3) are much smaller than in the atmosphere ($Re_{atm} \approx 10^6$–10^9), nevertheless, viscous effects are negligible in the laboratory, too. Another essential difference stems from the compressibility of the atmosphere: the air density at the tropopause is ∼40% of the surface value, while the corresponding difference in the towing tank cannot be larger than a few percents.

Two additional effects complicating the interpretation of results, which are not present in the real atmosphere, are described by Snyder et al. (1985). The first is the blocking phenomenon, where incompressible fluid piles up ahead of an obstacle altering permanently the upstream density profile. Elementary consideration of kinetic and potential energies of a parcel of fluid in a stratified environment gives a condition for blocking $2U/Nh < 1$. This predicts blocking in the laboratory for towing speeds $U < 0.5$–1 cm/s, and in the atmosphere for wind speeds $U < 10$ m/s. We observed indeed blocking for obstacle “C” (see Fig. 2) at very low towing speeds, but not for the other shapes in the range of interest of the experiments. As for the atmosphere, the crude estimate above completely neglects

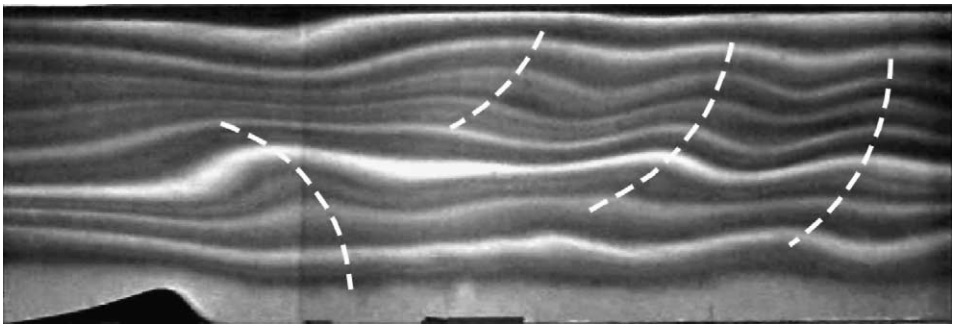

Fig. 3. Internal wave reflection from the top surface, dashed lines indicate propagating fronts (obstacle "D", $N = 1.33\,\mathrm{s}^{-1}$, $U = 4.2$ cm/s, $D = 36.8$ cm, $h/D = 0.11$).

compressibility and the three dimensional nature of orographic obstacles, which determine crucially the occurrence of upwind stagnation and blocking (Bauer et al., 2000).

The second effect results from the finite depth of the tank supporting upstream-propagating columnar modes. In the atmosphere, upward-propagating gravity waves radiate to infinity, whereas, in a towing tank, they can be reflected from the bottom or from the top free surface. Reflections from the top water surface were clearly observed in a few cases, an example is shown in Fig. 3. (Note that the top water surface was free, however, it can be considered as a rigid lid because of the large density difference and surface tension. Indeed, we never observed visible surface disturbances even at the largest amplitude internal waves.) In most cases, however, visible reflection was not present in the pattern field, especially in experiments with obstacles "A", "B" and "E" of smaller height ($h/D = 0.055$). Related experimental tests (Baines, 1977) indicate that the rigidity of upper boundary has a substantial effect at relative large obstacle heights $h/D > 0.15$. In spite of this, amplitudes and wavelengths were measured in our experiments for the first few wave-fronts only, in order to filter out possible interference effects.

2.3. Initial transients

In order to minimize the effects of initial transients, tests were performed to determine the necessary adjustment time t until a quasi-steady state was established. We found that a quasi-steady wave field was essentially built up when perturbations reached the top surface, if reflections could be neglected (as in most experiments). Thus, t should be inversely proportional to the vertical group velocity c_{gz} of propagating disturbances. The resulting waves were always standing in a frame comoving with the obstacle. Note, however, that the patterns are not necessarily identical with a final steady state configuration: numerical simulations by Lamb (1994) showed very long transients (up to 75 buoyancy periods), however, this meant only small amplitude departures from the initial patterns.

Experimentally, t was estimated by quickly playing the digitalized video-records (25 frames/s) forth and back several times. Since the observation of weak waves is partly subjective, an overall error of 10% seems to be reasonable.

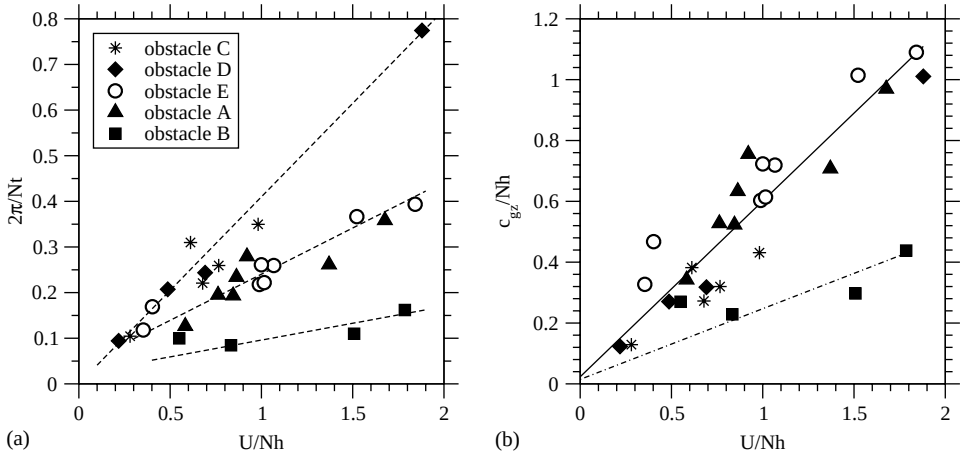

Fig. 4. (a) Inverse $2\pi/Nt$ of dimensionless adjustment time until a quasi-steady state was reached as a function of dimensionless towing speed U/Nh for three obstacles (obstacles "B" and "D" were towed with the broad side on leeward). Dashed lines indicate linear fits with slopes 0.41, 0.20 and 0.07, respectively. (b) Estimated vertical group velocity $c_{gz} = (D-h)/t$ as a function of towing speed U, both in units of Nh. The solid and dashed-dotted lines have slopes of 0.56 ± 0.04 and 0.23 ± 0.03, respectively.

In Fig. 4a, the inverse $2\pi/Nt$ of dimensionless adjustment time is plotted as a function of U/Nh for the different obstacles. The results indicate that 10–15 buoyancy periods were enough to build up a steady pattern even for the weakest perturbations represented by the low asymmetric obstacle "B" towed slowly with the broad side leeward. A linear relationship in Fig. 4a turned out to be a good approximation for each case. This means that the adjustment time t does not depend on the buoyancy frequency N. Since t obviously depends on the fluid depth D, we plotted in Fig. 4b the effective vertical group velocity c_{gz} estimated as $c_{gz} = (D-h)/t$. Most of the data seem to collapse onto a line of slope $\sim$1/2, outliers are the results for obstacle "B" towed with the gentle slope leeward. Note that Dupont et al. (2001) found in their experiments the same linear relationship $c_{gz} = mU$, even the constant of proportionality m was found to be close to one-half.

Data collapse in Fig. 4 suggests that t and thus c_{gz} are determined primarily by the towing velocity U for obstacles of large enough slopes, the height h and the buoyancy frequency N do not seem to be essential in our parameter range. For standing waves, the components of the group velocity must be strictly proportional to the towing speed (since it must vanish in a comoving frame), but the prefactor may depend on N through a (dimensionless) combination of the resultant wave vector components, which can neither be drawn nor visualized for an isolated ridge (Nappo, 2002). This prediction is based on linear theories, nevertheless, a comparison is supported by the fact that significant height dependence of c_{gz} was not observed. In order to experimentally resolve possible dependence of the adjustment time on N, one should measure the interval t very precisely at the same obstacle towed with the same speed in a wide range of N, but this is beyond the scope of the recent work. As for the significant deviation obtained with obstacle "B" (see Fig. 4b), we will return to this point in Section 4.

3. Results

It seems to be obvious that wave phenomena can be satisfactorily characterized by analysing amplitudes and wavelengths as a function of control parameters. However, this is strictly true only when self-similarity holds, such in the case of pure harmonic waves. Streamlines of lee-waves obey more complex, usually asymmetric shapes (see Fig. 5) , especially close to breaking. However, recent experimental work by Caulliez (2002) revealed self-similarity of wind blown near-breaking surface waves, and this kind of universality might also exist for internal waves. As a first approach, we determined the wavelength λ and amplitude A from the records as indicated in Fig. 5. In a few cases, we attempted to characterize quantitatively the asymmetry of waves by measuring the distances between a crest and appropriate left and right minima, the related results remained inconclusive.

By means of linear theory (Long, 1953, 1955; McIntyre, 1972), the wave field in a fluid of finite depth D can be decomposed into distinct modes $n = 1, 2, \ldots$ with a vertical wavenumber $k_z = n\pi/D$. Waves with horizontal wavenumber k_x have a horizontal group velocity $c_{gx} = Nk_z^2/(k_x^2 + k_z^2)^{3/2}$ which has a maximum for the first mode $n = 1$. The parameter K used in several works is this maximal group velocity divided by the upstream flow speed U

$$K = \frac{c_{gx}(n=1)}{U} = \frac{ND}{U\pi}. \tag{3}$$

If $K > 1$, there might exist mode-n waves ($n < K$) which are stationary with respect to the obstacle with horizontal wavenumber $k_x = \pi\sqrt{K^2 - n^2}/D$ or wavelength

$$\lambda = \frac{2D}{\sqrt{K^2 - n^2}}. \tag{4}$$

The obstacle height h is assumed to be very small, therefore it does not appear in the linear approximation. Note that different parametrizations incorporate h (Castro et al., 1983) or even the obstacle width w (Boyer and Tao, 1987) into the wavelength formula, but simple

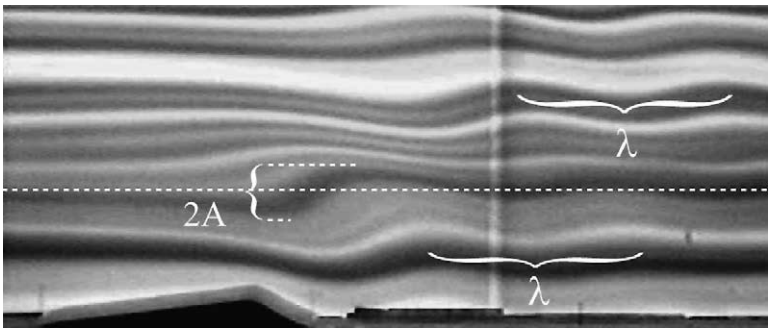

Fig. 5. Definition of measured lee-wave amplitude A and wavelength λ. Long dotted line indicates the position of an undisturbed streamline (obstacle "B", $U = 2.7$ cm/s, $N = 1.29\,\mathrm{s}^{-1}$, $D = 35$ cm).

algebra recovers Eq. (4) for each case. If $K \gg n$ holds, e.g. the fluid depth D is large enough, Eq. (4) gives the asymptotic estimate

$$\lambda \approx \frac{2\pi U}{N}, \tag{5}$$

which is equivalent with the so-called Scorer formula for height-independent buoyancy frequency N (Scorer, 1949).

There are no such simple equations for the amplitude and phase, since they strongly depend on the obstacle shape. An early study for atmospheric lee-waves over the "Witch of Agnesi" mountains was performed by Corby and Wallington (1956). In general, when results are based on first order perturbation theory, a linear amplitude variation with obstacle height h is expected. Furthermore, linear theory predicts that the lee-wave amplitude attains its maximum value at a given obstacle height when the obstacle half-width w is suitably adjusted to the natural wavelength of the flow field: $w = k_x^{-1}$. Baines (1979) measured amplitudes and phases for a series of obstacles and compared the results with linear theory. While the agreement for flat shapes was satisfactory, short obstacles produced significantly larger amplitudes than predicted.

3.1. Asymmetric obstacles

Following the milestone work by Baines and Hoinka (1985), we performed a series of experiments with the obstacles shown in Fig. 2 at several N and U values. The most essential differences between the two setups are that our characteristic aspect ratio h/D was smaller, and we did not implement the inclined top barrier invented by them in order to simulate radiative boundary condition. Figs. 6 and 7 show the results for wavelength and amplitude in two different representations. Note that plotted values indicate averages taken over a given picture, usually over the first few wave-fronts, thus error bars reflect nonuniformities as well. As expected, perturbation theory gives a lower limit both for wavelength and amplitude, especially for larger towing speeds.

Our results support the prediction of Lilly and Klemp (1979) and the qualitative observations of Baines and Hoinka (1985) that wavelength and amplitude are determined primarily by the shape of the lee-side: subsets produced by obstacles "A" and "B" (narrow side leeward), and "C" and "D" (narrow side leeward) cannot be distinguished, therefore they are denoted by the same symbols in Figs. 6 and 7. Some other predictions of linear theories seem to be realized, at least qualitatively: the wavelength does not depend strongly on the obstacle height, the amplitude is proportional to it, and both grow linearly for low towing velocities. Gentle leeward slopes generate significantly lower wave amplitudes, as expected. There is, however, an apparent wavelength anomaly for large enough flow rates: obstacles "B" and "D" towed with the wide side leeward produced lower wavelengths than in the opposite direction. Such behavior is not reported neither in the theoretical nor in the experimental literature; we return to this point in Section 4.

Note that a third possible representation for the data in Figs. 6 and 7 can be based on the inverse dimensionless towing velocity Nh/U. In general, the flow is linear if Nh/U is sufficiently small, nonlinearities (steepening, wave breaking and mixing, columnar disturbances, etc.) become increasingly important as Nh/U approaches and exceeds unity

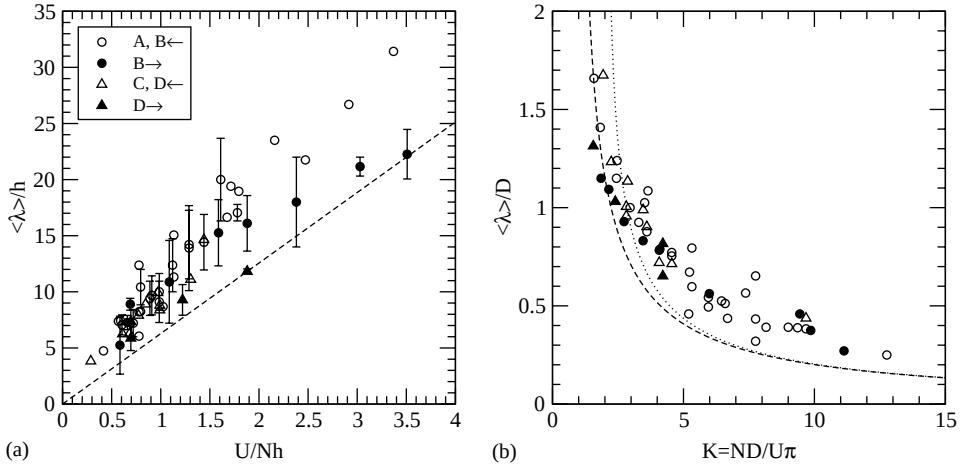

Fig. 6. (a) Average wavelength $\langle\lambda\rangle$ normalized by the obstacle height h as a function of dimensionless flow velocity U/Nh. Empty symbols denote symmetric ("A" and "C") and asymmetric ("B" and "D") obstacles towed with the steep side on leeward; filled symbols belong to asymmetric obstacles with the broad side on leeward. Dashed line indicates the theoretical line of Eq. (5), representative error bars are shown. (b) $\langle\lambda\rangle$ normalized by the total fluid depth D as a function of K (see Eq. (3)). Dashed and dotted lines indicate the theoretical prediction of Eq. (4) for $n = 1$ and 2, respectively.

(Baines, 1995). Since the fluid depth was essentially constant ($D = 35.0$–36.8 cm), plots as a function of parameter K (see Figs. 6b and 7b) contain basically the same information. The range of significant nonlinearities can be thus estimated as $K \gtrsim 3$ for $h = 4$ cm, and $K \gtrsim 6$ for $h = 2$ cm, respectively.

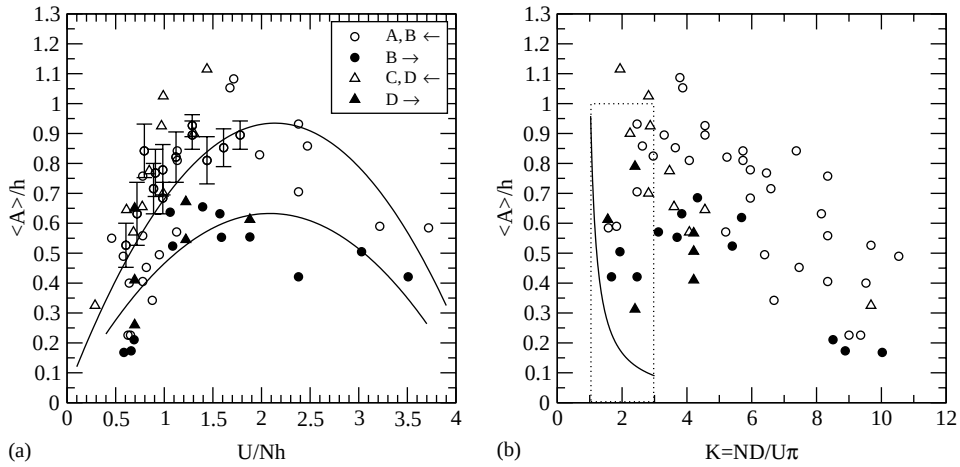

Fig. 7. (a) Average amplitude $\langle A\rangle$ normalized by the obstacle height h as a function of U/Nh, legends are the same as in Fig. 6. Quadratic fits are only to guide the eyes, representative error bars are shown. (b) $\langle A\rangle/h$ as a function of K. Dotted box indicate the range of experimental analysis by Baines (1979), his theoretical curve for $n = 1$ is shown by solid line.

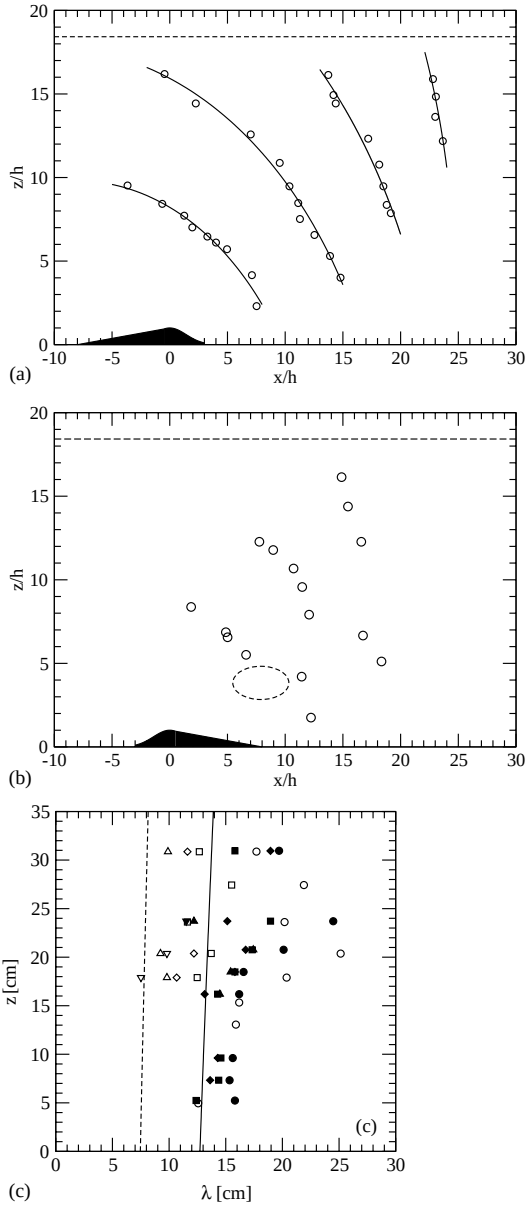

Fig. 8. (a) Location of wave maxima for obstacle "B", $U = 2.7$ cm/s, $N = 1.29\,\mathrm{s}^{-1}$, dashed line indicates the fluid surface, solid lines are fits by circle segments. (b) The same as (a), opposite flow direction. The dashed ellipse indicates the location of wave breakdown (rotor-like object). (c) Wavelength λ as a function of height z for two experiments with obstacle "B", short side leewards, $N = 1.29\,\mathrm{s}^{-1}$, $D = 35.0$ cm, $U_1 = 1.6$ cm/s (empty symbols), and $U_2 = 2.7$ cm (filled symbols). Different symbols identify the wave-fronts. Dashed and solid lines are theoretical estimates by Eq. (6) with U_1 and U_2, respectively.

As already mentioned, error bars in Figs. 6 and 7 reflect not only the limited resolution of digitized photographs but sometimes systematic dispersion of lee-waves. Linear theory predicts that wave-fronts (curves of constant phase) form circular sections centered at around the obstacle, which is rigorously valid for moving point sources (Voisin, 1994). Fig. 8a illustrates an example where circular fits could be obtained for wave maxima, however, the centers are gradually shifted to negative $(x/h, z/h)$ locations indicating stronger dispersion than expected. The standard explanation for wavelength dispersion is based on the fact that the fluid density decreases upward, thus Eq. (5) should be modified as

$$\lambda(z) \approx \frac{2\pi U}{N(z)}. \tag{6}$$

Theoretical lines in Fig. 8c show that the weakly decreasing density alone cannot elucidate the strong dispersion observed, which seems rather attributable to nonlinear effects.

Another difficulty for obstacles of gentle leeward slopes is illustrated in Fig. 8b. Although asymmetric wave patterns were typical in most of the experiments, total breakdown resulting in vertical vortices (rotor-like objects) was observed at low towing speeds with the wide sides leewards. Wave breakdown disturbs strongly the pattern field, sometimes it seems to act as secondary wave-source enhancing dispersion and interference.

3.2. Double bell-shaped obstacle

According to the simplest picture, a second obstacle placed at an odd number of half wavelengths downstream can exactly cancel lee-waves of the first obstacle, or the wave amplitude may be doubled due to a second obstacle one wavelength downstream of the first. Although the results for isolated obstacles indicate that linear predictions have limited

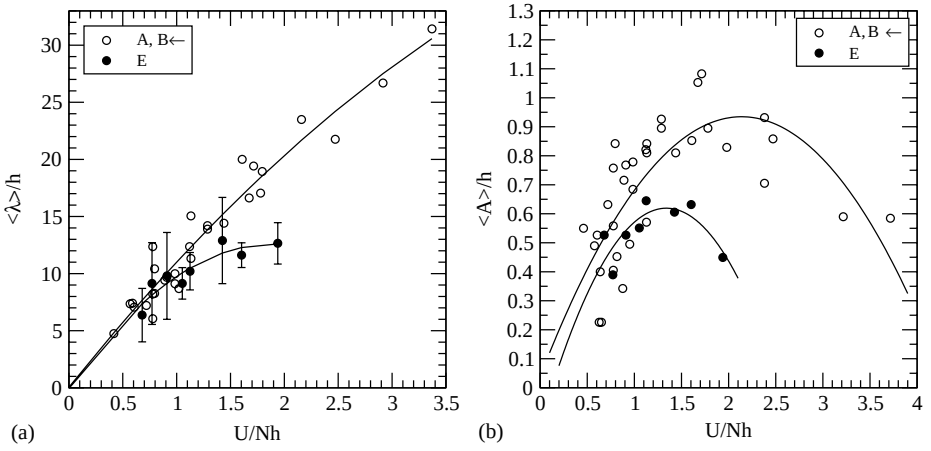

Fig. 9. Average wavelength $\langle\lambda\rangle$ (a) and average amplitude $\langle A\rangle$ (b) normalized by the obstacle height h as a function of dimensionless flow velocity U/Nh. Filled symbols belong to the double bell-shaped obstacle ("E"), empty symbols denote symmetric ("A") and asymmetric obstacles ("B") towed with the steep side on leeward. Representative error bars are shown. Quadratic fits (solid lines) only to guide the eyes.

applicability, we attempted to find experimentally lee-wave interference with a double bell-shaped obstacle. This was formed by joining up two obstacles "A" (see Fig. 2) at a peak-to-peak distance of 20.0 cm. The separation was chosen by considering the results of Fig. 6a: $\lambda_0 = 20$ cm is produced with a single obstacle ($h = 1.9$ cm) at around the towing speed $U/Nh \approx 1$, thus the available parameter range remains wide enough to cover a few multiples of half wavelength $\lambda_0/2$.

The results for the average wavelength and amplitude compared with the isolated obstacles are shown in Fig. 9. The breakdown of data for the double bell-shaped obstacle in the range $U/Nh > 2$ does not mean that there are no disturbances in the flow field (see Fig. 10, top). However, while patterns of an isolated obstacle (Fig. 10, bottom) can be easily characterized by amplitude and wavelength, similar quantities practically cannot be measured for the streamlines shown in Fig. 10 (top).

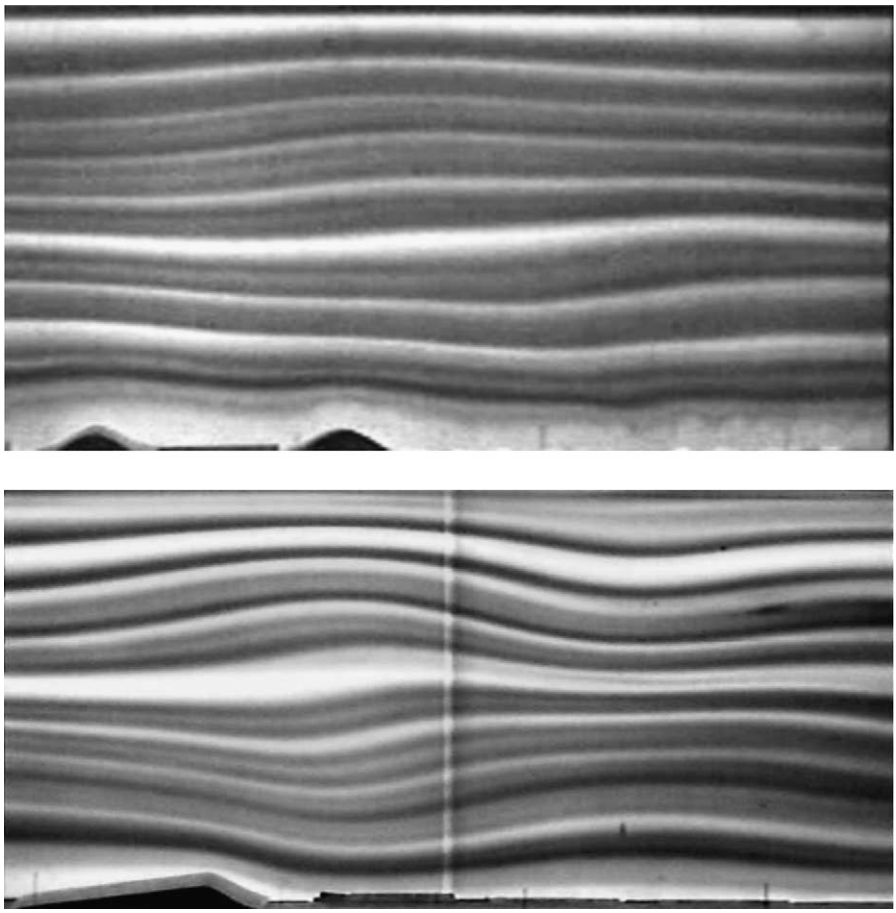

Fig. 10. Top: flow pattern at $U/Nh = 2.4$ for the double obstacle "E". Bottom: flow pattern at $U/Nh = 2.4$ for the isolated obstacle "B". Flow direction is from left to right for both cases.

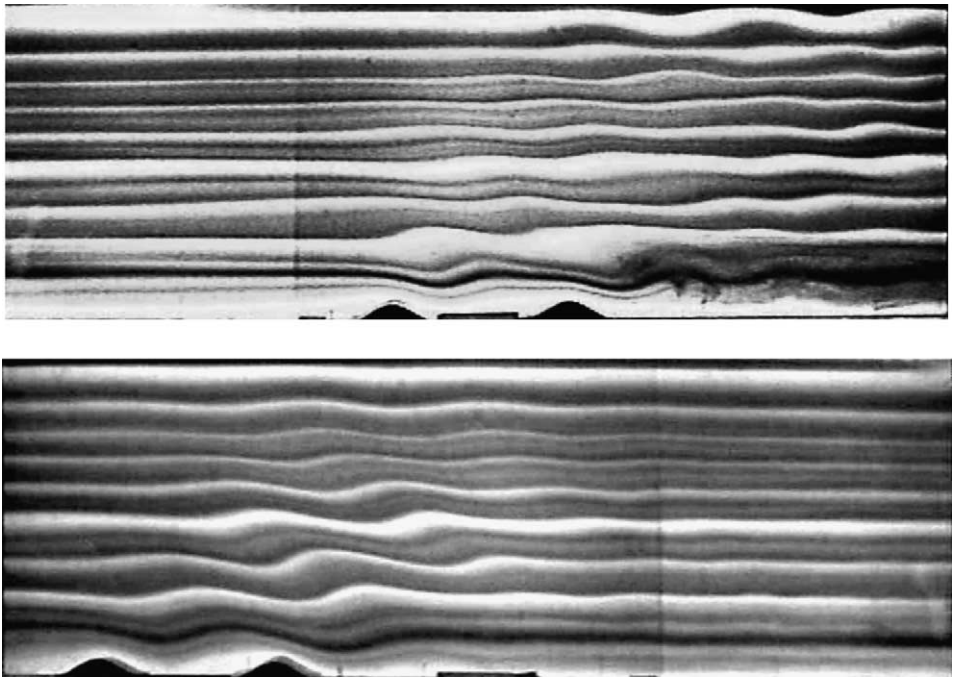

Fig. 11. Top: flow pattern at $U/Nh = 0.5$ for the double bell-shaped obstacle. Bottom: the same as above, $U/Nh = 1.0$, flow direction is from left to right.

It might seem surprising that constructive interference was essentially not observed. Fig. 11 illustrates two cases, where amplitude amplification were expected (wavelengths are $\lambda_0 \approx 10$ cm for $U/Nh = 0.5$, $\lambda_0 \approx 20$ cm for $U/Nh = 1.0$, while the peak-to-peak separation is 20 cm). In the first case (Fig. 11, top), the flow is well into the nonlinear regime, where the lower level fluid is partially blocked, particularly between the two obstacles. Amplification seems to result in strong turbulence after the second obstacle, and the pattern becomes quite irregular. In the second case (Fig. 11, bottom), amplitude doubling is not visible again, on the contrary: the waves remained localized at around the obstacles. Note that the pattern represents a quasi-steady wave-field for this experiments, not an early stage after the impulsive start. Interestingly, linear theory seems to fit qualitatively, at least the first wave-front behind the second obstacle has larger amplitude (and steeper slopes) than that behind the first. However, the fast decay of the wave-field is not consistent with linear superposition, it indicates the presence of significant nonlinear effects, such as the strong dispersion discussed at Fig. 8.

4. Discussion

Internal waves behind an isolated object are attributed to two origins: waves are generated because of buoyancy restoring forces acting on a parcel of fluid forced out of its equilibrium

depth, and because of the pressure gradient that develops in the lee. Sutherland (2002) performed experiments with "infinitely" asymmetric obstacles having a long plateau of constant height and a smooth sinusoidal leeward slope. This step-like geometry enhances the role of wave generation by pressure gradient forces. He identified stationary lee-waves trapped in the wake of the obstacle and vertically-propagating internal waves of slightly different frequencies but of the same amplitudes. Sutherland (2002) concluded that the dynamics are governed by nonhydrostatic nonlinear effects. Note that his parameter range $[U, N, H, h]$ was essentially the same as in our experiments. When the asymmetry of an obstacle is weaker, such in our case, the two wave-generating effects cannot be separated, but the concept gives a plausible mean for a qualitative explanation of our observations.

The relative contribution of buoyancy restoring forces and pressure gradient should be a (presumably complicated) function of the geometric aspect ratio, e.g. h/w_d, where w_d is the downstream half-width of the obstacle. Sutherland (2002) illustrated how the first term can be eliminated with $h/w_\mathrm{d} \approx 0$, but it seems plausible that the transition cannot be "infinitely" sharp: one should detect gradual (but certainly nonlinear) changes when h/w_d approaches zero. This simple argumentation might be related with the observed anomaly in Fig. 4. It is possible that the vertical group velocity $c_{\mathrm{g}z}$ changes visibly only below a particular aspect ratio (the asymmetry factor is $h/w_\mathrm{d} = 1.48$, 0.77, 0.53, and 0.25 for the obstacles "C", "A", "D", and "B", respectively).

The force that an obstacle exerts on the fluid through differential pressures on the windward and leeward slopes is known as the wave drag, and it is given by the integral along the surface of $p\,\mathrm{d}h(x)/\mathrm{d}x$, where $p = p(x, h)$ is the surface pressure, and the topography is given by $h(x)$. Lilly and Klemp (1979) pointed out that the wave drag and the wave amplitude are significantly enhanced for mountains with gentle windward and steep leeward slopes. Further, they found that the flow over an asymmetric obstacle with sharp downslope is qualitatively similar to that over the downslope side of a symmetric object. Both theoretical predictions are in agreement with our results (see Fig. 7). The same behavior for amplitudes was observed by Boyer and Tao (1987) for obstacles of (symmetric) triangular cross-sections: the smaller the aspect ratio (height/width), the lower the normalized amplitudes of lee-waves at the same towing speed. (They also noticed that a smooth object of cosine-square shape produced much larger waves than the sharp-edged triangular obstacle of the same aspect ratio.) In experiments with three-dimensional triangular ridges of changing spanwise width but of constant cross-section in a wide channel, Castro et al. (1983) observed the same trend as shown in Fig. 7a: after an approximately linear increase, normalized amplitudes decreased for towing velocities $U/Nh > 0.8$–1.0. Direct drag measurements by Castro et al. (1990) on quasi-two-dimensional obstacles revealed a rather complicated oscillatory dependence on U/Nh, however, the trend is unambiguously decreasing for each kind of objects at larger flow speeds. This observation suggests that lower wave amplitudes in this towing range could be associated with the reduced pressure gradient forces (wave drag). Different behavior was reported by Kadri et al. (1996). They found that the amplitudes decreased faster for objects of higher aspect ratios. However, they experimented with axi-symmetric Gaussian obstacles in a wide tank, where three-dimensional effects (roundabout flows) played an important role.

The observed wavelength anomaly, that obstacles of gentle leeward slopes generate lower wavelengths at large towing speeds (see Fig. 6a), cannot be explained easily by wave

drag arguments. Experimental papers report on good agreement with the linear predictions Eqs. (4) and (5) without significant influence from the object shape (Baines, 1979; Castro et al., 1983; Boyer and Tao, 1987; Kadri et al., 1996; Dupont et al., 2001). Note, however, that the dimensionless towing velocity in these experiments was restricted in the interval $U/Nh \in [0.1, 0.8]$, which is much closer to an assumed linear regime than in our experiments. In order to produce a data collapse in Fig. 6, one might naively assume that an effective buoyancy frequency N_{eff} exists over gentle leeward slopes, however, the desired transformation requires $N_{\text{eff}} < N$. Since there is no physical argument supporting such a picture, we can only conclude that nonlinear effects are responsible for the reduced wavelengths.

As for the interference of lee-waves, there is no related experiments published in the literature to our best knowledge. Sutherland (2001) performed experiments in uniformly salt-stratified fluid by towed two-dimensional periodic topography of finite extent. He reported on resonant interaction of waves from different origins resulting in constructive interference behind the moving obstacle. However, a periodic (sinusoidal) orography is very different from our obstacle "E", where the adjacent peaks have a much larger distance than their half-width w. Unfortunately, the theoretical works we found considered compressible atmospheric situations and concentrated on drag, blocking and breaking (Grisogono et al., 1993; Vosper, 1996; Mayr and Gohm, 2000), therefore a direct comparison with our observations is not possible. In a recent work, Vlasenko et al. (2002) studied tidally generated internal waves in a fjord over two adjacent sills by means of nonlinear numerical methods. Although the stratification and flow were not uniform in their model system, the second sill at the lee side of the first one generated much weaker internal waves than the first one resembling the fast decay of wave-field we have seen in our experiments (see Fig. 11). The pronounced wavelength and amplitude reduction (see Fig. 9), i.e. the lack of constructive interference is certainly different from what we expected. It is again a strong indication that nonlinear effects are dominating in the lee-wave generation process.

Acknowledgements

We would like to thank Mathew Wells for useful recommendations and Tamás Tél for several thorough discussions and for his permanent encouragement. We thank two anonymous referees for the constructive suggestions. This work was supported by the Hungarian National Science Foundation (OTKA) under grant no. T032423.

References

Baines, P.G., 1977. Upstream influence and Long's model in stratified flows. J. Fluid Mech. 82, 147–159.

Baines, P.G., 1979. Observations of stratified flow over two-dimensional obstacles in fluid of finite depth. Tellus 31, 351–371.

Baines, P.G., 1995. Topographic Effects in Stratified Flows. Cambridge University Press, Cambridge.

Baines, P.G., Granek, H., 1990. Hydraulic models of deep stratified flows over topography. In: Pratt, L.J. (Ed.), The Physical Oceanography of Sea Straits. Kluwer Academic Press, Dordrecht, pp. 245–269.

Baines, P.G., Hoinka, K.P., 1985. Stratified flow over two-dimensional topography in fluid of infinite depth: a laboratory simulation. J. Atmos. Sci. 42, 1614–1630.

Baines, P.G., Manins, P.C., 1989. The principles of laboratory modeling of stratified atmospheric flows over complex terrain. J. Appl. Meteorol. 28, 1213–1225.
Bauer, M.H., Mayr, G.J., Vergeiner, I., Pichler, H., 2000. Strongly nonlinear flow over and around a three-dimensional mountain as a function of the horizontal aspect ratio. J. Atmos. Sci. 57, 3971–3991.
Boyer, D.L., Tao, L., 1987. Impulsively started, linearly stratified flow over long ridges. J. Atmos. Sci. 44, 23–42.
Castro, I.P., Snyder, W.H., Marsh, G.L., 1983. Stratified flow over three-dimensional ridges. J. Fluid Mech. 135, 261–282.
Castro, I.P., Snyder, W.H., Baines, P.G., 1990. Obstacle drag in stratified flow. Proc. R. Soc. Lond. A 429, 119–140.
Caulliez, G., 2002. Self-similarity of near-breaking short gravity wind waves. Phys. Fluids 14, 2917–2920.
Corby, G.A., Wallington, C.E., 1956. Airflow over mountains: the lee-wave amplitude. Q. J. R. Meteorol. Soc. 82, 266–274.
Dupont, P., Kadri, Y., Chomaz, J.M., 2001. Internal waves generated by the wake of Gaussian hills. Phys. Fluids 13, 3223–3233.
Fortuin, J., 1960. Theory and application of two supplementary methods of constructing density gradient columns. J. Polym. Sci. 44, 505–515.
Garner, S.T., 1995. Permanent and transient upstream effects in nonlinear stratified flow over a ridge. J. Atmos. Sci. 52, 227–246.
Grisogono, B., Pryor, S.C., Keislar, R.E., 1993. Mountain wave drag over double bell-shaped orography. Q. J. R. Meteorol. Soc. 119, 199–206.
Kadri, Y., Bonneton, P., Chomaz, J.M., Perrier, M., 1996. Stratified flow over three-dimensional topography. Dyn. Atmos. Oceans 23, 321–334.
Lamb, K.G., 1994. Numerical simulations of stratified inviscid flow over a smooth obstacle. J. Fluid Mech. 260, 1–22.
Lilly, D.K., Klemp, J.B., 1979. The effects of terrain shape on nonlinear hydrostatic mountain waves. J. Fluid Mech. 95, 241–261.
Long, R.R., 1953. Some aspects of the flow of stratified fluids. I. A theoretical investigation. Tellus 5, 42–58.
Long, R.R., 1955. Some aspects of the flow of stratified fluids. III. Continuous density gradients. Tellus 7, 341–357.
Lyra, G., 1943. Theorie der stationaren Leewellwenströmung in freien Atmosphäre. Z. Angew. Math. Mech. (Berlin) 23, 1–28.
Mayr, G.J., Gohm, A., 2000. 2D airflow over a double bell-shaped mountain. Meteorol. Atmos. Phys. 72, 13–27.
McIntyre, M.E., 1972. On Long's hypothesis of no upstream influence in uniformly stratified or rotating flow. J. Fluid Mech. 52, 209–243.
Nappo, C.J., 2002. An Introduction to Atmospheric Gravity Waves. Academic Press, San Diego.
Qiu, X.-L., Xia, K.-Q., 1998. Viscous boundary layers at the sidewall of a convection cell. Phys. Rev. E 58, 486–491.
Queney, P., 1948. The problem of airflow over mountains: a summary of theoretical studies. Bull. Am. Meteorol. Soc. 29, 16–25.
Röttger, J., 2000. ST radar observations of atmospheric waves over mountainous areas: a review. Ann. Geophys. 18, 750–765.
Scorer, R.S., 1949. Theory of waves in the lee of mountains. Q. J. R. Meteorol. Soc. 75, 41–56.
Scorer, R.S., 1978. Environmental Aerodynamics. Ellis Horwood, Chichester.
Snyder, W.H., Thompson, R.S., Eskridge, R.E., Lawson, R.E., Castro, I.P., Lee, J.T., Hunt, J.C.R., Ogawa, Y., 1985. The structure of strongly stratified flow over hills: dividing streamline concept. J. Fluid Mech. 152, 249–288.
Sutherland, B.R., 2001. Internal wave generation in the lee of periodic topography. In: Proceedings of the Presentation at the 54th Annual Meeting of the APS Division of Fluid Dynamics, San Diego, CA, 18–20 November.
Sutherland, B.R., 2002. Large-amplitude internal wave generation in the lee of step-shaped topography. Geophys. Res. Lett. 29, 15321–15325.
Turner, J.S., 1979. Buoyancy Effects in Fluids. Cambridge University Press, Cambridge.
Vlasenko, V., Stashchuk, N., Hutter, K., 2002. Water exchange in fjords induced by tidally generated internal lee waves. Dyn. Atmos. Oceans 35, 63–89.
Voisin, B., 1994. Internal wave generation in uniformly stratified fluids. Part 2. Moving point sources. J. Fluid Mech. 261, 333–374.
Vosper, S., 1996. Gravity-wave drag on two mountains. Q. J. R. Meteorol. Soc. 122, 993–999.
Whelan, R.F., 2000. Exploring the Monster. Mountain Lee Waves: The Aerial Elevator. Wind Canyon Books, Brawley.